Journal of Agricultural Engineering

https://www.agroengineering.org/

Discrete element modeling of bivalve *Mactra veneriformis*: parameter calibration and mechanized harvesting validation

Hangqi Li,[1,2*] Bin Xu,[1,3*] Hao Wu,[1,2] Xiaodong Lv,[1] Yuzhong Lou,[1] Xiuchen Li,[1,4] Guochen Zhang,[1,2,4] Gang Mu[1,4]

[1]College of Mechanical and Power Engineering, Dalian Ocean University, Dalian
[2]College of Engineering, Shenyang Agricultural University, Shenyang
[3]College of Mechanical and Electrical Engineering, Harbin Engineering University, Harbin
[4]Liaoning Provincial Marine Fishery Equipment Specialized Technology Innovation Center, Dalian, China

Corresponding Authors: Guochen Zhang, College of Mechanical and Power Engineering, Dalian Ocean University, Dalian 116023, China. E-mail: zhangguochen_dlou@163.com
Gang Mu, College of Mechanical and Power Engineering, Dalian Ocean University, Dalian 116023, China. E-mail: mugang@dlou.edu.cn

Publisher's Disclaimer

E-publishing ahead of print is increasingly important for the rapid dissemination of science. The *Early Access* service lets users access peer-reviewed articles well before print/regular issue publication, significantly reducing the time it takes for critical findings to reach the research community.
These articles are searchable and citable by their DOI (Digital Object Identifier).

Our Journal is, therefore, e-publishing PDF files of an early version of manuscripts that undergone a regular peer review and have been accepted for publication, but have not been through the typesetting, pagination and proofreading processes, which may lead to differences between this version and the final one.
The final version of the manuscript will then appear on a regular issue of the journal.

Please cite this article as doi: 10.4081/jae.2026.2193

©The Author(s), 2026
Licensee PAGEPress, Italy

Submitted: 19 March 2026
Accepted: 26 October 2026

***Note**: The publisher is not responsible for the content or functionality of any supporting information supplied by the authors. Any queries should be directed to the corresponding author for the article.*

All claims expressed in this article are solely those of the authors and do not necessarily represent those of their affiliated organizations, or those of the publisher, the editors and the reviewers. Any product that may be evaluated in this article or claim that may be made by its manufacturer is not guaranteed or endorsed by the publisher.

Discrete element modeling of bivalve *Mactra veneriformis*: parameter calibration and mechanized harvesting validation

Hangqi Li,[1,2*] Bin Xu,[1,3*] Hao Wu,[1,2] Xiaodong Lv,[1] Yuzhong Lou,[1] Xiuchen Li,[1,4] Guochen Zhang,[1,2,4] Gang Mu[1,4]

[1]College of Mechanical and Power Engineering, Dalian Ocean University, Dalian

[2]College of Engineering, Shenyang Agricultural University, Shenyang

[3]College of Mechanical and Electrical Engineering, Harbin Engineering University, Harbin

[4]Liaoning Provincial Marine Fishery Equipment Specialized Technology Innovation Center, Dalian, China

[*]These authors contributed equally to this work and share first authorship

Corresponding authors:
Guochen Zhang, College of Mechanical and Power Engineering, Dalian Ocean University, Dalian 116023, China. E-mail: zhangguochen_dlou@163.com
Gang Mu, College of Mechanical and Power Engineering, Dalian Ocean University, Dalian 116023, China. E-mail: mugang@dlou.edu.cn

Authors' contributions: **Hangqi Li**: Writing, Validation, Software, Data curation, Conceptualization; **Gang Mu**: Writing – review & editing, Funding acquisition, Conceptualization; **Bin Xu:** Software, Validation experiment; **Hao Wu**: Software; **Xiaodong Lv**: Validation experiment; **Yuzhong Lou**: Validation. **Guochen Zhang**: Writing – review & editing, Funding acquisition, Conceptualization; **Xiuchen Li**: Funding acquisition, Conceptualization.

Conflict of interest: The authors declare that they have no known competing financial interests or personal relationships that could have appeared to influence the work reported in this paper.

Data Availability Statement: The original contributions presented in the study are included in the article, further inquiries can be directed to the corresponding authors.

Funding: This research was funded by the National Key R&D Program of China, Grant Number 2023YFD2400800.The Basic Scientific Research Program of Liaoning Provincial Education Department, Grant Number LJ232410158048. Liaoning Provincial Undergraduate Colleges and Universities Basic Scientific Research Operational Fees Program, Grant number

2024JBPTZ002. Dalian Science and Technology Innovation Fund, Grant number 2024JJ13GX039.

Acknowledgments: The authors thank the editor and anonymous reviewers for providing helpful suggestions for improving the quality of this manuscript. Thanks Qian Zhang, Hanbing Zhang, Mingjin Xin, Yutong Cheng, all the teachers and classmates for their help and support.

Abstract

To reduce mudflat disturbance caused by hydraulic dredging and facilitate efficient, environmentally responsible mechanized harvesting of buried bivalves, this study aimed to develop an accurate discrete element method (DEM) model for analyzing *Mactra veneriformis* (*M. veneriformis*)–machine interactions and optimizing harvesting parameters. The geometry of *M. veneriformis* was reconstructed using three-dimensional scanning and represented in EDEM using a multi-sphere model. The Edinburgh elasto-plastic adhesion (EEPA) model was used to describe *M. veneriformis–M. veneriformis* interactions. Physical experiments were used to determine the static friction and restitution coefficients for *M. veneriformis*–stainless steel contacts and the restitution coefficient for *M. veneriformis–M. veneriformis* contacts, while DEM simulations were used to calibrate the remaining contact parameters. The angle of repose (AOR) was measured using the cylinder-lifting method and selected as the macroscopic response for DEM calibration. A Plackett–Burman design followed by a Box–Behnken design was used to screen and optimize the influential contact parameters. The rolling friction coefficient, static friction coefficient, and surface energy of *M. veneriformis–M. veneriformis* contacts were identified as the principal factors affecting the AOR. The optimized values were 0.05, 0.30, and 2 J m^{-2}, respectively. Using these parameters, the simulated AOR was 23.17°, with a relative error of 4.09% relative to the physical experiment. The calibrated model was subsequently applied to mechanized harvesting simulations and validated against field harvesting tests, reproducing the principal trends observed under field conditions. The validated DEM model provides a basis for analyzing *M. veneriformis*–machine interactions and optimizing mechanized harvesting systems, while the proposed modeling and calibration framework may also support DEM studies of other bivalves.

Key words: *Mactra veneriformis*; discrete element method; parameter calibration; angle of repose; mechanized harvesting

Introduction

The shellfish aquaculture industry forms the backbone of China's fisheries sector. In 2023, China's shellfish aquaculture production reached approximately 1.65×10^7 tons, representing 28.67% of the total aquaculture output (Bureau of Fisheries, 2024) and making a substantial contribution to national and regional economies. *Mactra veneriformis* (*M. veneriformis*), a commercially important bivalve of the family Mactridae, is widely distributed across intertidal mudflats. During the harvesting season, it typically inhabits sandy-silty sediments at burial depths of approximately 30–50 mm, with harvesting mainly occurring from April to September. The species has high production and considerable economic value. Harvesting is a pivotal process in mudflat shellfish farming, as its efficiency directly affects both yields and economic returns. The two primary methods for harvesting mudflat shellfish are manual harvesting and hydraulic dredging. Although hydraulic dredging is more efficient, it has been banned due to its adverse environmental impacts, poor selectivity, and the increased risk of shellfish mortality from sand inhalation (Mu *et al*., 2020; Yang, 2022; Ministry of Agriculture and Rural Affairs of the People's Republic of China, 2013). Manual harvesting, by contrast, is labor-intensive and expensive. Developing an efficient and environmentally sustainable mechanized harvester is now an urgent priority. The Discrete Element Method (DEM), extensively applied in agricultural mechanization research (Zhao *et al*., 2023; Li *et al*., 2024), serves as an effective tool for studying the complex motion of *M. veneriformis* during mechanized harvesting. Developing an accurate DEM model for the *M. veneriformis* enhances the simulation and precision of its mechanized harvesting, providing a necessary foundation for optimizing harvesting equipment design and advancing the mechanized harvesting of *M. veneriformis*, promoting the development of aquacultural engineering.

DEM modeling and contact-parameter calibration have been extensively studied for agricultural granular materials. DEM contact parameters are generally determined either by direct measurement (Shi *et al*., 2019) or through simulation-based calibration. However, some contact parameters are difficult to measure directly, and geometric simplification may cause experimentally measured material properties to differ from their effective DEM values. Consequently, calibration against measurable macroscopic responses has been widely adopted in DEM studies of agricultural particulate materials (Coetzee, 2016). The angle of repose (AOR) is widely used as a macroscopic response for DEM calibration because it reflects the combined effects of particle geometry, friction, and rolling resistance on bulk flow and accumulation behavior. This calibration approach has been applied to a wide range of agricultural materials,

including *Panax notoginseng* (notoginseng) (Yu *et al*., 2020), rice (Liu *et al*., 2023), potatoes (Liu *et al*., 2018), wheat (Liu *et al*., 2016), apples (Zhang *et al*., 2024), peanuts (Wu *et al*., 2020), maize grain (Ligier *et al*., 2024), and *Cyperus esculentus* (tiger nut) (Chen *et al*., 2023).

In contrast, DEM studies of bivalves remain relatively limited. Li *et al.* (2021) and Lou *et al.* (2024) developed DEM models for juvenile *Ruditapes philippinarum* (Manila clam) and *M. veneriformis*, respectively, using the Hertz–Mindlin no-slip contact model. These studies primarily considered dry contact conditions, in which bivalve motion is governed mainly by friction, rolling, and collision. However, *M. veneriformis* is mechanically harvested from wet mudflat sediments, where bivalve–sediment and bivalve–machine interactions are considerably more complex. Under these conditions, water and fine sediment retained on shell surfaces contribute to shell–sediment adhesion, shell–stainless steel adhesion, and aggregate formation. Consequently, *M. veneriformis* motion during harvesting is governed not only by friction and impact but also by interfacial adhesion, sediment retention, aggregate breakup, and detachment from sediment and machine surfaces. These wet cohesive and adhesive interactions cannot be adequately represented by contact parameters calibrated solely under dry conditions. Therefore, experiments conducted under wet conditions provide a more representative basis for modeling *M. veneriformis*–sediment–machine interactions during mechanized harvesting.

The Edinburgh elasto-plastic adhesion (EEPA) model accounts for elastoplastic deformation and adhesive forces and has been widely applied to cohesive particulate materials (Thakur *et al*., 2014). The EEPA model has been applied to cohesive soils under different moisture conditions (Xie *et al*., 2020; Janda and Ooi, 2016; Wu *et al*., 2021; Wanli *et al*., 2021), as well as to silt loam (Zhao *et al*., 2024), sandy soil (Mo *et al*., 2024), sandy loam (Li *et al.,* 2023), animal feed (Sun *et al*., 2024), and peat (Wang *et al*., 2024). These applications support the suitability of the EEPA model for representing cohesive and adhesive particle interactions. Accordingly, applying the EEPA model to wet cohesive *M. veneriformis* harvesting provides a means of representing shell–shell, shell–sediment, and sediment–sediment interactions that are difficult to capture using conventional dry-contact models.

This study aimed to develop and validate a DEM model of *M. veneriformis* under wet cohesive harvesting conditions. Stainless steel was selected as the primary material for key harvesting components because of its resistance to seawater corrosion. A three-dimensional shell model was constructed using 3D scanning and the multi-sphere model (MSM), and directly measurable contact parameters were determined through physical experiments. A sequential Plackett–Burman design (PBD) and Box–Behnken design (BBD) were then used to identify the DEM parameters with significant main effects on the AOR of *M. veneriformis* and to determine

the parameter combination that minimized the discrepancy between the simulated and physical AOR. The calibrated model was subsequently applied to DEM–multibody dynamics (MBD) coupled harvesting simulations and validated against field mudflat harvesting tests. This study provides a methodological framework for analyzing *M. veneriformis*–machine interactions and may also inform DEM modeling of other bivalves under similar wet cohesive conditions. In addition, the physical and mechanical properties of the mudflat sediment before and after mechanized harvesting were comparatively evaluated. Sediment density, water content, shear strength at different depths, and penetration resistance were measured to quantify harvesting-induced changes in sediment structure and mechanical conditions, thereby assessing the disturbance caused by mechanized harvesting to the mudflat sediment environment.

Materials and Methods

Physical parameters of *M. veneriformis*

M. veneriformis specimens (Figure 1a) used in this study were collected from intertidal and nearshore mudflat aquaculture areas in Panjin City, Liaoning Province, China (121°8′56″E, 40°42′4″N). The specimens had been cultured for at least 3 years and met the local harvest-size criterion of no more than 40 individuals per 500 g. Fifty specimens meeting this criterion were randomly selected for subsequent physical measurements. The length (l_1), height (l_2), and width (l_3) of the shellfish were measured using digital vernier calipers (Guanglu Digital Measurement and Control Co., Ltd., 111-101-10G, China). The volume (v_C) was measured using a 100 mL cylinder and the water-drainage method, while the mass (m_C) was determined using an electronic balance (Minqiao Precision Technology Co., Ltd., CN0340, China). The shellfish density (ρ_C) was then calculated.

M. veneriformis DEM modeling

M. veneriformis was scanned using a three-dimensional scanner (POP2, Zhixiang Optoelectronics Technology Co., Ltd., China). The point-cloud data were denoised and repaired in Geomagic Studio (Geomagic Studio 2016, Geomagic, USA) to reconstruct a complete shell surface, which was then checked to confirm that it was closed and watertight (Figure 1b). The reconstructed geometry was imported into EDEM (2022, Altair Inc., USA), where the automatic filling function generated an 18-sphere MSM (Figure 1c). The MSM preserved the principal shell dimensions, volume, and mass while maintaining computational efficiency for harvesting-scale simulations. Fine-scale features such as growth lines and local surface roughness were not explicitly resolved; their effects on macroscopic contact behavior were

instead incorporated indirectly through experimentally calibrated effective contact parameters. The 18-sphere MSM was therefore adopted for subsequent DEM simulations. The Edinburgh elasto-plastic adhesion (EEPA) model was used for *M. veneriformis–M. veneriformis* contacts (Sun *et al*., 2024), whereas the Hertz–Mindlin with JKR model was applied to *M. veneriformis*–stainless steel contacts (Li *et al*., 2019).

M. veneriformis contact parameter measurements

M. veneriformis–stainless steel static friction coefficient

The static friction coefficient between *M. veneriformis* and stainless steel was measured using the inclined-plate method with a digital inclinometer (Ruifen Technology Co., Ltd, DMI410, China). A 304 stainless steel plate was used as the inclined surface, and the *M. veneriformis* was placed horizontally on it. The lifting platform was gradually raised until the clam began to slide, and the inclination angle at this point, α_s, was recorded. Thirty independent specimens were tested to account for inter-individual variation in shell morphology and shell–plate contact orientation (Li *et al*., 2026), and the average static friction coefficient, $\mu_{s\text{-}C\text{-}S}$, was calculated using formula (1).

$$\mu_{s\text{-}C\text{-}S} = \tan \alpha_s \quad \text{(Eq. 1)}$$

M. veneriformis–stainless steel restitution coefficient

The restitution coefficient between *M. veneriformis* and stainless steel was measured using a free-fall bounce experiment. The *M. veneriformis* was lifted to a height of 150 mm (H_0) and allowed to free-fall onto a stainless steel base plate, with coordinate paper used as a background. The collision and rebound were recorded using a high-speed video camera (640×480 pixels@100fps, Insight Technology, OSG030-790UM, China). The highest rebound height (H_1) was measured, the test was independently repeated thirty times using different specimens (Lou *et al.,* 2025), and the restitution coefficient between *M. veneriformis* and stainless steel was calculated using formula (2).

$$e_{C\text{-}S} = \sqrt{\frac{H_1}{H_0}} \quad \text{(Eq.2)}$$

The stainless-steel plate tests were used to calibrate the effective shell–stainless steel contact parameters under controlled conditions rather than to reproduce the complete shell–machine interaction occurring during harvesting.

M. veneriformis–M. veneriformis restitution coefficient

The restitution coefficient between *M. veneriformis* was measured using a collision experiment (Liu *et al*., 2018). Two *M. veneriformis* were suspended by 160 mm-long wires, anchored at one end to a fixed bracket. *M. veneriformis* A was suspended at rest, with its suspension point as the origin, while *M. veneriformis* B has been elevated to a position 30 mm higher than *M. veneriformis* A. Upon release, *M. veneriformis* B swung and collided with *M. veneriformis* A. The collision was recorded using a high-speed video camera (640×480 pixels@100fps), and the elevation difference between *M. veneriformis* A and B post-collision was measured as *30* mm (Figure 2 a-c). The experiment was repeated thirty times, and the average value was used to calculate the restitution coefficient, $e_{C\text{-}C}$, of *M. veneriformis* using formula (3).

$$e_{C\text{-}C} = \frac{\sqrt{H_3} - \sqrt{H_2}}{\sqrt{30}} \qquad \text{(Eq. 3)}$$

AOR

The AOR of *M. veneriformis* (θ_C) reflects the combined effects of geometric interlocking, friction, and rolling resistance during gravity-driven flow and accumulation and was therefore selected as the calibration response. The AOR was measured using the cylinder-lifting method. Two hundred specimens were placed in a stainless-steel cylinder (164 mm in diameter) on a stainless-steel base plate(Figure 3a). After lifting the cylinder, the dimensions of the resulting pile (length, width, and height) were measured using rulers mounted on the base plate and frame, and the pile was recorded from the front, top, and side views using a fixed camera. The images were processed in MATLAB (MATLAB 2022, MathWorks, USA) by grayscale conversion, binarization, image segmentation, and edge extraction (Figure 3 c-f) to obtain the pile boundary profiles. The extracted boundary data were then imported into Origin (Origin 2022, OriginLab, USA), where the boundary points were fitted using the measured pile dimensions as spatial references to determine the slope and corresponding AOR (Figure 3g). The cylinder-lifting experiment was independently repeated ten times, yielding over thirty measured AOR values to calculate the mean response.

Impact-induced breakage force

To quantify impact-induced fracture resistance, a drop-to-failure experiment was conducted following Zhang *et al*. (2025) (Figure 4). Ten *M. veneriformis* specimens were subjected to free-fall drop tests onto a stainless-steel base plate from progressively increasing heights. The minimum drop height at which complete shell fracture occurred in all ten specimens was

defined as the critical fracture height. During each test, specimens were released with the shell-width side facing downward, ensuring impact with the base plate along the shell-width direction. The drop height was controlled using a graduated scale, and the impact and fracture processes were recorded using a high-speed camera. The critical fracture height (H_4), mean specimen mass (m_C), and collision duration (Δt) were then used to estimate the breakage force ($F_{b–C}$) according to Eqs. (4)–(7).

Assuming free fall from rest and neglecting air resistance, the impact velocity immediately before collision was calculated as:

$$v_C = \sqrt{2gH_4} \quad \text{(Eq. 4)}$$

The mean impact force during shell–plate collision was then estimated using the impulse–momentum relationship:

$$F_{i\text{-}C} = \frac{m_C v_C}{\Delta t} \quad \text{(Eq. 5)}$$

The gravitational force acting on the specimen was calculated as:

$$G_C = m_C g \quad \text{(Eq. 6)}$$

Accordingly, the resultant force at the critical fracture condition was defined as the breakage force:

$$F_{b\text{-}C} = F_{i\text{-}C} + G_C \quad \text{(Eq. 7)}$$

where v_C is the impact velocity immediately before collision, m s^{-1}; H_4 is the critical fracture height, m; g is the gravitational acceleration, m s^{-2}; $F_{i–C}$ is the mean impact force during shell–plate collision, N; m_C is the mean mass of *M. veneriformis*, kg; Δt is the collision and fracture duration, approximately 0.01 s; G_C is the gravitational force acting on the specimen, N; and $F_{b–C}$ is the resultant breakage force, N.

Calibration of simulated contact parameters

Simulated contact parameters calibration

Single-factor DEM simulations of *M. veneriformis* were conducted in EDEM using the corresponding physical measurements as calibration targets. The ranges of the target contact parameters were estimated from the physical measurements and divided into five evenly spaced levels to characterize the parameter–response relationships and support least-squares regression. At each parameter level, five independent runs were performed using randomly generated initial shell configurations to account for variability in the initial contact state. The mean response at each level was used for regression analysis, and simulation reproducibility was assessed using the coefficient of variation (*CV*) across the five independent runs.

The *M. veneriformis*–stainless steel static-friction and free-fall rebound simulations replicated the configurations used in the corresponding physical experiments. For the *M. veneriformis–M. veneriformis* collision simulation, *M. veneriformis* A and B were placed in a smooth, frictionless cylinder (320 mm in diameter), with *M. veneriformis* B positioned at the bottom. *M. veneriformis* A was released along the inner wall from an initial vertical height of 30 mm above *M. veneriformis* B and allowed to collide with it. The vertical height difference between *M. veneriformis* A and B after collision (H_3) was recorded (Figure 2 d-f). To isolate the effect of the target parameter, the non-target contact parameters were set to zero where applicable (Hanley *et al*., 2011; Grima *et al*., 2011).

The relationships between the target contact parameters and the corresponding simulation responses were fitted by least-squares linear regression (Ucgul *et al*., 2014). A coefficient of determination of $R^2 \geq 0.90$ was used as the criterion for acceptable regression fitting. The calibrated contact parameters were then reintroduced into the corresponding DEM models, and their validity was evaluated by comparing the simulated responses with the physical measurements using the relative error (δ).

***M. veneriformis* stacking PBD simulation**

Under wet and adhesive conditions, several contact and EEPA model parameters of *M. veneriformis* cannot be determined directly using conventional physical measurements. Therefore, a PBD was employed to screen the DEM parameters with significant main effects on the AOR (θ_C), which served as the response variable. PBD enables multiple candidate parameters to be screened with a limited number of simulation runs and has been widely applied to DEM parameter calibration (Wu *et al*., 2021; Xiang *et al*., 2019; Yan *et al*., 2022). A PBD comprising eight actual DEM factors: Factor A was the surface energy for *M. veneriformis–M. veneriformis* contacts, representing the adhesive strength at shell–shell interfaces; higher values increase resistance to separation and promote transient adhesion or agglomeration. Factor B was the contact plasticity ratio for shell–shell contacts, characterizing the contribution of irreversible deformation during loading and unloading, with higher values indicating greater plastic dissipation and weaker rebound. Factor C was the tension factor for shell–shell contacts, which controls the tensile resistance of adhesive contacts during separation. Factor D was the tangential stiffness multiplier for shell–shell contacts, which scales the tangential contact stiffness and influences tangential displacement and resistance to relative sliding. Factor E was the rolling friction coefficient for *M. veneriformis*–stainless steel contacts, representing resistance to rolling at the shell–steel interface. Factors F and G were the static and rolling

friction coefficients, respectively, for *M. veneriformis–M. veneriformis* contacts, representing resistance to shell sliding and rolling. Factor H was the surface energy for *M. veneriformis*–stainless steel contacts, characterizing adhesive interactions at the shell–steel interface, and three dummy factors were generated using Design-Expert 13 (Stat-Ease Inc., USA). The factor ranges were selected based on previous DEM calibration studies (Wu *et al*., 2021; Zhao *et al*., 2024; Li *et al*., 2023; Sun *et al*., 2024).

***M. veneriformis* stacking BBD simulation**

Based on the AOR PBD simulation results, a three-factor, three-level AOR BBD simulation was designed (Zhao *et al*., 2024; Boikov *et al*., 2019). In this simulation, the AOR of *M. veneriformis* was selected as the response value, while the DEM model parameters with insignificant effects were fixed at their intermediate levels. A second-order regression model between the AOR and the significant factors was developed using Design-Expert software. The optimal simulation contact parameter combinations for the *M. veneriformis* DEM model, closest to the physical AOR, were obtained through optimized solving. Five center-point runs were included in the BBD to estimate pure error and assess experimental reproducibility.

DEM–MBD harvesting simulation and field validation

To validate the accuracy of the DEM model of *M. veneriformis*, a mudflat harvesting verification simulation was conducted, using the shell breakage rate as the evaluation indicator. A DEM model of *M. veneriformis*–mudflat sediments was developed based on cultured mudflat conditions. The Edinburgh Elasto-Plastic Adhesion (EEPA) model (Wu *et al*., 2021) was used for contact interactions between mudflat sediment particles, while the Hertz-Mindlin with JKR model (Xiang *et al*., 2019; Li *et al*., 2019) was applied for interactions between mudflat sediments and stainless steel. The model parameters are listed in Table S1 and Table S2 (Li *et al*., 2026).

The mechanized harvester for *M. veneriformis* on mudflats consists primarily of a first-stage vibrating shovel sieve, a second-stage vibrating sieve, a first-stage double-spiral harvesting roller brush, and a second-stage sieving roller brush. The entire harvester is diesel-powered and self-propelled with wheels. During harvesting, the front-end excavating shovel of the first-stage vibrating sieve penetrates the mudflat for vibration-based excavation. The first-stage double-spiral harvesting roller brush assists in breaking and pushing the sediments backward. The first and second-stage vibrating sieves work in coordination with their respective roller brushes to separate shellfish from sediments. Harvested clams meeting size requirements are conveyed to

the collection basket, while sediment and undersized clams fall through the sieve.

To improve computational efficiency, a DEM environment representing the mudflat habitat for *M. veneriformis* cultivation was established in EDEM, where material properties and contact parameters were specified. The substrate domain was set to 200 mm × 105 mm × 80 mm and populated with 10 *M. veneriformis* clams and 34,000 sediment particles. A simplified 3D model of the mechanized harvester was imported into RecurDyn. The vibrating-screen working width and harvesting depth were set to 100 mm and 60 mm, respectively. In RecurDyn, joint definitions, and operating conditions were prescribed, including a forward speed of 0.1 $m \cdot s^{-1}$, vibration frequencies of 13 Hz for both first-stage and second-stage screens, and rotational speeds of 48 $r \cdot min^{-1}$ and 96 $r \cdot min^{-1}$ for the first-stage double-spiral harvesting brush and the second-stage screening brush, respectively. The bristles of both roller brushes were modeled as flexible bodies and discretized *via* meshing. The equipment surfaces were then exported as rigid wall geometries using the External function to generate the coupled model, which was imported into the EDEM mudflat environment to perform the coupled DEM–MBD simulation of the mechanized harvesting process (Figure 5a).

During post-processing, the Manual Selection tool and Grid Bin Group monitoring modules in EDEM were used to (i) record the contact forces acting on each clam individual at each time step and (ii) quantify the masses of collected clams and retained mudflat sediment in the collection device. Force–time histories were extracted for each clam to identify fracture events and calculate the simulated breakage rate (δ'_B). A clam was classified as fractured when its maximum contact force exceeded 9.1 N, facilitating qualitative assessment of force distributions and the shell-breaking process. The mud-attachment ratio on the shell surface ($W'_{C\text{-}M}$) was further determined from the measured masses of sediment and clams retained in the collector. Collectively, these outputs provide quantitative evidence for evaluating harvesting performance and optimizing the structure and operating parameters of the harvesting equipment.

During the field test of mechanized harvesting of *M. veneriformis* in mudflats, operating parameters of the mechanical harvester—such as screen vibration frequency, roller brush rotation speed, harvesting depth, and travel speed—were adjusted accordingly. A field harvesting test was then conducted on the mudflat using the same Operating parameters (Figure 5b). For every 5 meters of travel, the number of harvested *M. veneriformis*, the number of broken individuals, and the breakage rate (δ_B) were recorded. Thirty *M. veneriformis* individuals were randomly selected from the harvested samples. The mass of each clam together with the mudflat sediment adhered to its surface was first measured. The clams were then washed and the shell surfaces were wiped dry, after which the clean clam mass was measured.

The mud-attachment ratio on the shell surface ($W_{C\text{-}M}$) was calculated accordingly. The test was repeated 5 times, and the average values were used to validate the model's accuracy.

Mudflat sediment properties before and after harvesting

To assess harvesting-induced disturbance to the mudflat sediment, its physical and mechanical properties were measured at the same locations before and after mechanized harvesting (Figure 5e). Surface sediment samples were collected using a core cutter and aluminum containers. Sample mass was measured using an electronic balance, and sediment wet density (ρ_S) was calculated from the sample mass and core volume. The samples were then oven-dried at 100 °C for 12 h (DHG-9245A, Shanghai Yiheng Scientific Instrument Co., Ltd., China) until samples mass are stable, and water content (W_w) was determined from the mass loss after drying. Each measurement was independently replicated five times.

Sediment shear strength (τ_S) was measured at depths of 50, 70, and 100 mm using a vane shear tester (VST-3M, Suzhou Tuoce, China). In addition, because the mudflat sediment was relatively soft, penetration resistance (F_R) was measured at depths of 50, 100, and 150 mm using a penetration resistance tester (DJ-200, Tianjin Shouke Experimental Instrument Co., Ltd., China) to characterize changes in sediment resistance to mechanical disturbance before and after harvesting.

Results

Physical parameters of *M. veneriformis*

The measured physical and contact parameters of *M. veneriformis* are summarized in Table 1. The static friction coefficient ($\mu_{s\text{-}C\text{-}S}$) was 0.32, whereas the restitution coefficients for *M. veneriformis*–stainless steel (e_{CS}) and *M. veneriformis–M. veneriformis* (e_{CC}) contacts were 0.28 and 0.29, respectively. Except for the rebound heights H_1 and H_3, the coefficients of variation (CVs) of the measured physical and contact parameters of *M. veneriformis* were below 15%, indicating relatively low variability. In contrast, H_1 and H_3 exhibited relatively high CVs of 27.97% and 29.25%, respectively. This variability was likely associated with the irregular, approximately ellipsoidal shell geometry, which resulted in differences in contact orientation and impact location and, consequently, greater variation in rebound behavior. At the critical drop height (H_4) of 1300 mm, the breakage force ($F_{b\text{-}C}$) was estimated to be 9.1 N.

Calibration results of simulated contact coefficient

Calibration results of directly measured contact coefficient

The single-factor calibration results for *M. veneriformis*–stainless steel static friction and restitution, together with *M. veneriformis–M. veneriformis* restitution, are shown in Figure 6. At each parameter level, the mean response from five independent simulations was used for regression fitting, with error bars indicating the variability among replicate runs. The fitted relationships y_1, y_2, and y_3 in Eq. (8) yielded coefficients of determination of $R^2_1 = 0.99$, $R^2_2 = 0.99$, and $R^2_3 = 0.98$, respectively, indicating good agreement between the fitted relationships and the simulation data. The corresponding physical measurements were then substituted into the fitted equations, yielding calibrated DEM contact parameters of $\mu'_{s\text{-}C\text{-}S} = 0.30$, $e'_{C\text{-}S} = 0.32$, $e'_{C\text{-}C} = 0.26$. These calibrated parameters were subsequently reintroduced into the corresponding DEM models for validation, and comparisons between the physical measurements and simulated responses are summarized in Table 2. Overall, the calibrated DEM models reproduced the corresponding static-friction and rebound responses observed in the physical experiments, with relative errors ranging from 2.93% to 14.50%.

$$\begin{cases} y_1 = 54.15x + 1.86 \\ y_2 = 2.23x + 0.95 \\ y_3 = 39.80x - 0.80 \end{cases} \quad \text{(Eq. 8)}$$

M. veneriformis stacking PBD simulation

The definitions, contact pairs, factor levels, and corresponding PBD matrix are summarized in Table 3. Based on the PBD simulation results for the AOR of *M. veneriformis* (Table S3), the standardized effects of the candidate DEM parameters are shown in the Pareto chart in Figure 7. Three factors were identified as significant: G: the *M. veneriformis–M. veneriformis* rolling friction coefficient; F: the *M. veneriformis–M. veneriformis* static friction coefficient; and A: the *M. veneriformis–M. veneriformis* surface energy. The remaining factors were not significant and were therefore fixed at their intermediate levels, while G, F, and A were retained for subsequent BBD optimization. The non-significant factors were fixed at B = 0.40, C = 3.00, D = 0.60, E = 0.175, and H = 1.05 J·m^{-2}.

M. veneriformis AOR BBD simulation

Based on the BBD simulation design and results for the AOR of *M. veneriformis* (Table 4), a regression model linking the AOR to three significant parameters was established using the analysis function of Design Expert software, yielding its polynomial equation (Eq. 10). ANOVA

analysis of the regression model (Table 5) revealed that the effects of G (rolling friction coefficient) and F (static friction coefficient) on the AOR of *M. veneriformis* were highly significant, while the effect of A (surface energy) was also significant. As shown in Table 5, the relationship between the dependent and independent variables in the regression model was highly significant ($p<0.001$), with a good model precision (*Adeq Precision* = 6.0261). The misfit term was insignificant ($p=0.5981$), with a coefficient of determination R^2 = 0.9202 and an adjusted R^2 = 0.8724, indicating that the fitted equation is reliable. The coefficient of variation *C.V.* = 3.43% further supports the reliability of the simulation. The *M. veneriformis* stacking BBD simulation can be used to predict the AOR. The interaction between G and F significantly affected the AOR ($p=0.0099$).

$$\theta_s = 27.07 + 2.60A + 2.16B - 0.800C + 1.53AB + 0.1988AC - 0.3788BC \quad \text{(Eq. 9)}$$

Optimal parameter combination and simulation verification

Using the physical AOR of *M. veneriformis* ($\theta_C = 22.26°$) as the target, Design-Expert software was used to determine the optimal parameters for the *M. veneriformis* DEM model. The results were: G = 0.05, F = 0.30, and A = 2 J·m^{-2}. The simulation verification yielded a AOR of θ'_C=23.17°, with a relative error of δ_θ = 4.09%. There was no significant difference between the DEM simulation and physical results (Figure 3 a,b).

Validation results of mechanized harvesting simulation

The coupled DEM–MBD simulation reproduced the principal harvesting responses observed in the field experiment. The simulated breakage rate was 5.00%, compared with 8.75% in the field tests, giving an absolute difference of 3.75 percentage points. The simulated shell surface mud-attachment ratio (W'_{CM}) was 2.87%, compared with a measured field value (W_{CM}) of 3.05%. Overall, the simulation reproduced shell damage and surface mud attachment at levels comparable to those measured under field harvesting conditions.

Mudflat sediment properties before and after harvesting

Changes in the physical and mechanical properties of the mudflat sediment before and after mechanized harvesting are summarized in Table 6. After harvesting, wet bulk density decreased from 1892.78 ± 53.47 to 1747.22 ± 62.22 kg m^{-3}, corresponding to a reduction of 7.69%, whereas water content changed only slightly, from 34.00 ± 4.89% to 33.27 ± 2.53%. The response of sediment shear strength to harvesting varied with depth. Shear strength decreased by 5.92% and 10.23% at depths of 50 and 70 mm, respectively, whereas it remained nearly

unchanged at 100 mm, with an increase of only 1.86%. In contrast, penetration resistance exhibited substantially larger changes following mechanized harvesting. After harvesting, penetration resistance decreased to 0 N at depths of 50 and 100 mm and from 17.43 ± 0.97 to 1.60 ± 0.33 N at 150 mm, corresponding to a reduction of 90.82% at the latter depth. Overall, mechanized harvesting produced relatively small changes in sediment water content and shear strength but more pronounced reductions in sediment density and penetration resistance.

Discussion

Mechanized harvesting of *M. veneriformis* under wet mudflat conditions involves complex shell–shell, shell–sediment, and shell–machine interactions that are difficult to characterize experimentally. In this study, physical measurements were combined with DEM parameter calibration and coupled DEM–MBD harvesting simulations to establish and validate a numerical model of *M. veneriformis*. The shell–shell rolling friction coefficient, static friction coefficient, and surface energy were identified as the principal parameters affecting the AOR, and the calibrated model reproduced the measured AOR with a relative error of 4.09%. The model also captured the principal trends in shell breakage and surface mud attachment observed during field harvesting. Meanwhile, reductions in sediment density and penetration resistance indicated that mechanized harvesting mainly caused short-term loosening of the mudflat sediment. These findings provide the basis for interpreting the calibrated model, evaluating shell–machine interactions, and discussing the applicability and limitations of mechanized harvesting under wet mudflat conditions.

Influence of contact parameters on the AOR

The GF interaction was further examined using response surface analysis in Design-Expert. As shown in Figure 8, the AOR increased as both G and F increased. When either G or F increased individually, the AOR increased gradually, indicating a comparatively limited effect of either friction mechanism alone on shell accumulation. In contrast, simultaneous increases in G and F produced a stronger increase in the AOR, suggesting a synergistic effect of rolling and static friction that restricted shell sliding and rearrangement during pile formation. The quasi-rectangular to broad-ovate shell morphology of *M. veneriformis* may facilitate tumbling and reorientation, which may partly explain its relatively low resistance to rolling. During vibratory harvesting, screen inclination may promote reverse shell sliding toward the feed end, thereby reducing conveying stability and separation efficiency. Accordingly, introducing anti-slip surface features, such as patterned roughness, may increase shell–screen interfacial friction and

tangential traction, thereby reducing reverse sliding.

Compared with earlier calibrations conducted under the Hertz-Mindlin no-slip contact model, rolling friction for both clam–clam and clam–stainless steel contacts was reported to have a highly significant effect on the AOR, while clam–clam static friction was significant–consistent with the present response surface results and reinforcing the dominant role of frictional parameters in describing shellfish piling behavior (Lou *et al.*, 2025). In contrast, calibration under the EEPA model indicates that surface energy should also be considered. Introducing surface energy enables a more realistic representation of inter–shell adhesion, thereby improving model fidelity under moist or mildly adhesive conditions. Notably, previously reported values (rolling friction 0.23, static friction 0.41 for clam–clam, and rolling friction 0.16 for clam–stainless steel) are overall higher than those obtained here, suggesting that when adhesion is explicitly included, energy dissipation shifts from purely frictional losses to a combined mechanism involving friction, adhesion, and plastic deformation, which is more consistent with the physical behaviour of the system.

Relative to the DEM calibration for juvenile Manila clam under the Hertz-Mindlin no-slip model, both inter-particle rolling/static friction and juvenile–stainless steel rolling friction were also reported as highly significant for the AOR (Li *et al*., 2021), in agreement with the present findings. However, the calibrated values (μ_s = 1.25 and μ_r = 0.33) were markedly higher than those obtained for clam. This discrepancy may partly arise from differences in shell morphology and surface characteristics between the two species. Juvenile Manila clams generally have flatter shells with more pronounced surface ornamentation, which may increase geometric interlocking and resistance to sliding and rolling. In contrast, clam shells are closer to a triangular/trapezoidal symmetry with thicker shells and comparatively smoother surfaces, characterised by coarser ribs and sparser growth lines, which reduces rolling and sliding resistance. These comparisons highlight that species-specific morphology and surface features should be explicitly considered in shellfish DEM modelling to improve the accuracy of predicted motion and piling behaviour.

Harvesting validation and model applicability

The lower breakage rate predicted by the simulation may be partly attributable to simplifications in the numerical model. The screening assembly was represented using idealized geometry and assembly conditions, which did not fully reproduce localized squeezing, repeated impacts, and manufacturing or assembly deviations present in the actual machine. Consequently, some fracture events observed in the field, particularly those occurring at sieve junctions and

during discharge into the collection basket, were underrepresented in the simulation. Nevertheless, the model captured the principal trends in shell breakage and surface mud attachment, supporting its use for analyzing major *M. veneriformis*–machine interactions and for comparative evaluation of harvesting parameters. Predictions of localized shell fracture should, however, be interpreted with caution.

Effects of mechanized harvesting on mudflat sediment properties

The reductions in sediment density and penetration resistance, together with the relatively stable water content, suggest that the harvesting-induced changes in sediment properties were primarily associated with structural disturbance rather than changes in moisture conditions (Figure 5 c,d). Excavation, vibration, and screening during harvesting may disrupt the original particle arrangement and interparticle contact network, resulting in a looser sediment structure with lower compactness and penetration resistance. The reduction in shear strength at 50 and 70 mm, together with the negligible change at 100 mm, suggests that harvesting-induced changes in shear resistance were more evident in the shallower sediment layers. Notably, penetration resistance at 150 mm decreased by 90.82%, indicating that this parameter was particularly responsive to harvesting-induced changes in sediment structure. The looser sediment conditions after harvesting may also facilitate the re-burrowing of juvenile clams returned to the mudflat surface; however, this potential ecological implication requires direct verification through re-burrowing experiments.

For comparison, previous measurements following hydraulic harvesting reported penetration resistances of 12.8, 35.8, and 95.4 N at depths of 50, 100, and 150 mm, respectively, considerably higher than the corresponding pre-harvesting values measured in the present study (1.57, 5.71, and 17.43 N) (Li *et al*., 2022). At 150 mm, the penetration resistance reported after hydraulic harvesting (95.4 N) was approximately 5.47 and 59.63 times the before and after mechanized-harvesting values measured in the present study, respectively. The high penetration resistance reported after hydraulic harvesting is consistent with sediment hardening, whereas mechanized harvesting in the present study reduced penetration resistance below the pre-harvesting level at all measured depths. These contrasting responses suggest that hydraulic and mechanized harvesting may produce distinct patterns of sediment physical disturbance. Taken together, the changes in sediment density, water content, shear strength, and penetration resistance indicate that the immediate physical effect of mechanized harvesting was primarily a loosening of the sediment structure. Such conditions may facilitate juvenile clam re-burrowing; however, whether the disturbed sediment subsequently recovers under tidal

processes, and the rate and ecological consequences of such recovery, require further evaluation through time-series monitoring.

Model limitations and future improvements

The 18-sphere MSM represented the overall shell geometry with reduced computational cost; however, fine-scale morphological features, including local curvature and surface roughness, were not explicitly resolved. Their combined effects were therefore represented indirectly through the calibrated effective contact parameters. In addition, the shell was treated as a rigid body, preventing the model from representing crack initiation, propagation, and progressive fracture. This limitation is particularly relevant to the prediction of localized shell damage. Wet-condition effects were represented through adhesion-related contact parameters rather than explicit fluid modeling; consequently, hydrodynamic effects and moisture-dependent changes in sediment behavior were not directly resolved.

Future work should therefore focus on improving both shell-fracture representation and wet-condition modeling. A bonded DEM shell model could be developed to simulate progressive fracture and quantify shell damage severity, while incorporating morphological and mechanical variability among *M. veneriformis* specimens from different aquaculture regions. In parallel, a more detailed wet-adhesive *M. veneriformis*–sediment model should be calibrated across multiple sediment water contents for shell–sediment, sediment–sediment, and sediment–stainless steel interactions. These improvements would help quantify moisture-dependent contact behavior and extend the applicability of the model across different mudflat harvesting conditions.

Conclusions

This study developed and validated a DEM model of *M. veneriformis* for mechanized harvesting under wet mudflat conditions. The shell-shell rolling friction coefficient, static friction coefficient, and surface energy were identified as the principal parameters affecting the AOR, with optimized values of 0.05, 0.30, and 2 J m^{-2}, respectively. The calibrated model reproduced the measured AOR with a relative error of 4.09% and captured the principal trends in shell breakage and surface mud attachment observed during field harvesting. These results support the application of the calibrated model to the analysis of *M. veneriformis*–machine interactions and the comparative evaluation of harvesting parameters.

Mechanized harvesting reduced mudflat sediment wet bulk density by 7.69% and substantially decreased penetration resistance, whereas water content and shear strength changed relatively

little. These changes indicate that the immediate physical effect of mechanized harvesting was primarily sediment loosening rather than pronounced hardening. These findings suggest that mechanized harvesting has potential as a lower-disturbance alternative to hydraulic harvesting and may support more sustainable mudflat bivalve aquaculture.

References

Bureau of Fisheries, 2024. 2024 China Fisheries Statistical Yearbook. Beijing, China Agriculture Press.

Boikov AV, Savelev RV, Payor VA, et al., 2019. DEM calibration approach: Orthogonal experiment. J Phys Conf Ser 1210:012025.

Chen Y, Gao XX, Jin X, Ma X, Hu B, Zhang H, 2023. [Calibration and analysis of seeding parameters of Cyperus esculentus seeds based on discrete element simulation].[Article in Chinese with English Abstract]. Trans Chin Soc Agric Mach 54:58-69.

Coetzee CJ, 2016. Calibration of the discrete element method and the effect of particle shape. Powder Technol 297:50-70.

Grima AP, Wypych PW, 2011. Development and validation of calibration methods for discrete element modelling. Granul Matter 13:127-132.

Hanley KJ, O'Sullivan C, Oliveira JC, Cronin K, Byrne EP, 2011. Application of Taguchi methods to DEM calibration of bonded agglomerates. Powder Technol 210:230-240.

Hao JJ, Wei WB, Huang PC, Qin J, Zhang J, 2021. [Calibration and experimental verification of discrete element parameters of oil sunflower seeds].[Article in Chinese with English Abstract]. Trans Chin Soc Agric Eng 37:36-44.

Hou ZF, Dai NZ, Chen Z, Qiu Y, Zhang XW, 2020. [Measurement and calibration of physical property parameters for Agropyron seeds in a discrete element simulation].[Article in Chinese with English Abstract]. Trans Chin Soc Agric Eng 36:46-54.

Janda A, Ooi JY, 2016. DEM modeling of cone penetration and unconfined compression in cohesive solids. Powder Technol 293:60-68.

Li HQ, 2022. [Dynamic simulation and experimental studies on vibration harvesting equipment for tidal buried shellfish].[PhD Thesis in Chinese]. Dalian Ocean University.

Li HQ, Mu G, Xu B, Chen GC, Zhang GC, Li XC, 2026. Multi-response calibration and validation of a DEM for wet Mactra veneriformis–mudflat sediment mixtures during mechanised harvesting. Biosyst Eng 270:104558.

Li HQ, Zhang GC, Li XC, Zhang HB, Zhang Q, Liu WB, Mu G, 2021. Calibration of the discrete element method parameters in living juvenile Manila clam (Ruditapes philippinarum) and seeding verification. AgriEngineering 3:894-906.

Li HQ, Zhang GC, Liu FW, Li XC, Wang Y, Mu G, 2024. [Design and testing of mudflat shellfish vibrating harvester based on DEM-MBD simulation].[Article in Chinese with English Abstract]. Trans Chin Soc Agric Mach 55:361-370.

Li SC, Diao PS, Zhao YL, Miao HQ, Li XH, Zhao HD, 2023. Calibration of discrete element parameter of soil in high speed tillage. INMATEH Agric Eng 71:248-258..

Li JW, Tong J, Hu B, Wang HB, Mao CY, Ma YH, 2019. [Calibration of parameters of interaction between clayey black soil with different moisture content and soil-engaging component in northeast China].[Article in Chinese with English Abstract]. Trans Chin Soc Agric Eng 35:130-140.

Li YX, Li FX, Xu XM, 2019. [Parameter calibration of wheat flour for discrete element method simulation based on particle scaling].[Article in Chinese with English Abstract]. Trans Chin Soc Agric Eng 35:320-327.
Liu DW, Duan JP, Chen XY, Xiong ZK, Wang SX, Xie PF, 2023. [Calibration of friction parameters of seed particle models of hybrid rice based on EDEM].[Article in Chinese with English Abstract]. J Shenyang Agric Univ 54:189-195.
Liu FY, Zhang J, Li B, Chen J, 2016. [Calibration of parameters of wheat required in discrete element method simulation based on repose angle of particle heap].[Article in Chinese with English Abstract]. Trans Chin Soc Agric Eng 32:247-253.
Liu WZ, He J, Li HW, Li WQ, Zheng K, Wei ZC, 2018. [Calibration of simulation parameters for potato minituber based on EDEM].[Article in Chinese with English Abstract]. Trans Chin Soc Agric Eng 49:125-135.
Lou YZ, Zhang GC, Li XC, Zhang Q, Zhang HB, Zhao JJ, et al., 2025. Experiment and calibration of contact parameters of Mactra veneriformis based on DEM. Comput Part Mech 12:313-326.
Ministry of Agriculture and Rural Affairs of the People's Republic of China, 2013. Notice from the Ministry of Agriculture on the prohibition of thirteen types of fishing gear, including double-vessel single-net multi-pocket trawls. Document [EB/OL].2013-11-19.
Mo HT, 2024. [Simulation and experiment on impeller soil interaction of boat-tractor].[PhD Thesis in Chinese]. Wuhan, Huazhong Agricultural University.
Mu G, Duan FH, Yang JY, Zhang HB, Li XC, Pan LL, et al., 2020. [Research progress on burying shellfish harvesters: A review].[In Chinese with English abstract]. J Dalian Ocean Univ 35:19-30.
Shi LR, Ma ZT, Zhao WY, Wang XP, Sub BG, Zhang JP, 2019. [Calibration of simulation parameters of flaxed seeds using discrete element method and verification of seed-metering test].[In Chinese with English abstract]. Trans Chin Soc Agric Eng 35:25-33.
Sun WF, Sun Y, Wang Y, He HM, 2024. Calibration and experimental verification of discrete element parameters for modelling feed pelleting. Biosyst Eng 237:182-195.
Thakur SC, Morrissey JP, Sun J, Chen JF, Ooi JY, 2014. Micromechanical analysis of cohesive granular materials using the discrete element method with an adhesive elasto-plastic contact model. Granul Matter 16:383-400.
Ucgul M, Fielke JM, Saunders C, 2014. Three-dimensional discrete element modelling of tillage: Determination of a suitable contact model and parameters for a cohesionless soil. Biosyst Eng 121:105-117.
Wang BB, He Z, Ding XT, Hao W, Yang Z, Cui YJ, 2024. [Calibration of peat discrete element parameters based on uniaxial closed compression test].[In Chinese with English abstract]. Trans Chin Soc Agric Mach 55:87-97.
Wanli PC, Li YL, Su C, Zhao H, Dong XQ, Song JN, Wang JC, 2021. [Simulation of soil tillage characteristics and influence analysis of particle sphere type based on EEPA contact model].[In Chinese with English abstract]. J China Agric Univ 26:193-206.
Wu MC, Cong JL, Yan Q, Zhu T, Peng XY, Wang YS, 2020. [Calibration and experiments for discrete element simulation parameters of peanut seed particles.[In Chinese with English abstract]. Trans Chin Soc Agric Eng 36:30-38.
Wu ZY, Wang XD, Liu DW, Xie FP, Ashwehmbom LG, Zhang ZH, Tang Q, 2021. Calibration of discrete element parameters and experimental verification for modelling subsurface soils. Biosyst Eng 212:215-227.
Xiang W, Wu ML, Lv JN, Quan W, Ma L, Liu JJ, 2019. [Calibration of simulation physical parameters of clay loam based on soil accumulation test].[In Chinese with English abstract]. Trans Chin Soc Agric Eng 35:116-123.
Xie FP, Wu ZY, Wang XS, Liu DW, Wu B, Zhang ZZ, 2020. [Calibration of discrete element

parameters of soils based on unconfined compressive strength test].[In Chinese with English abstract]. Trans Chin Soc Agric Eng 36:39-47.
Yan DX, Yu JQ, Wang Y, Zhou L, Tian Y, Zhang N, 2022. Soil particle modeling and parameter calibration based on discrete element method. Agriculture 12:1421.
Yang HS, 2022. [Current status and prospects of scientific and technological innovation in modern fisheries].[Book in Chinese]. Beijing, Science Press.
Yu QX, Liu Y, Chen XB, Sun K, Lai Q, 2020. [Calibration and experiment of simulation parameters for Panax notoginseng seeds based on DEM].[In Chinese with English abstract]. Trans Chin Soc Agric Mach 51:123-132.
Zhang G, Li Z, Liu W, Zhang Q, Chen L, Pei L, et al., 2025. [Finite element simulation and experiment of impact damage of water chestnuts].[In Chinese with English abstract]. Trans Chin Soc Agric Eng 41:40-49.
Zhang GZ, Chen LM, Liu HP, Dong Z, Zhang Q, Zhou Y, 2022. [Calibration and experiments of the discrete element simulation parameters for water chestnut].[In Chinese with English abstract]. Trans Chin Soc Agric Eng 38:41-50.
Zhang HJ, Han X, Yang HW, Chen XB, Zhao GZ, Sun JW, et al., 2024. [Calibrating and simulating contact parameters of the discrete element for apple particles].[In Chinese with English abstract]. Trans Chin Soc Agric Eng 40:66-76.
Zhao JL, Lu Y, Wang XG, Zhuang J, Han Z, 2023. A bionic profiling-energy storage device based on MBD-DEM coupled simulation optimization reducing the energy consumption of deep loosening. Soil Tillage Res 234:105824.
Zhao JW, Yu JQ, Sun K, Wang Y, Liang LS, Sun YX, et al., 2024. A discrete element method model and experimental verification for wheat root systems. Biosyst Eng 244:146-165.

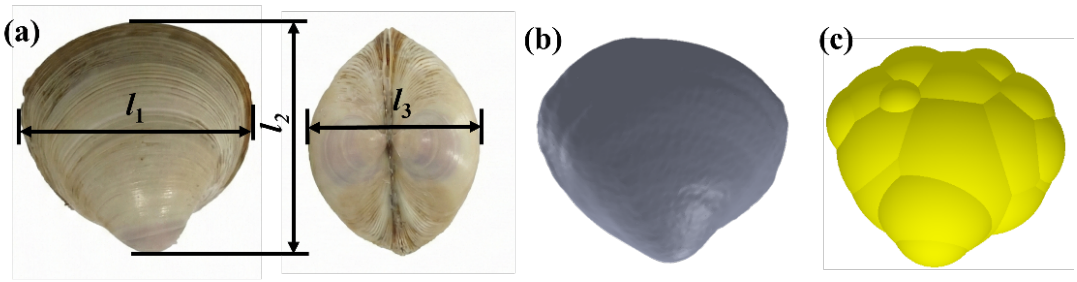


Figure 1. Construction of the *M. veneriformis* DEM model. **a)** *M. veneriformis*. **b)** 3D scanned shell geometry. **c)** DEM model. l_1, shellfish length; l_2, shellfish height; l_3, shellfish width.

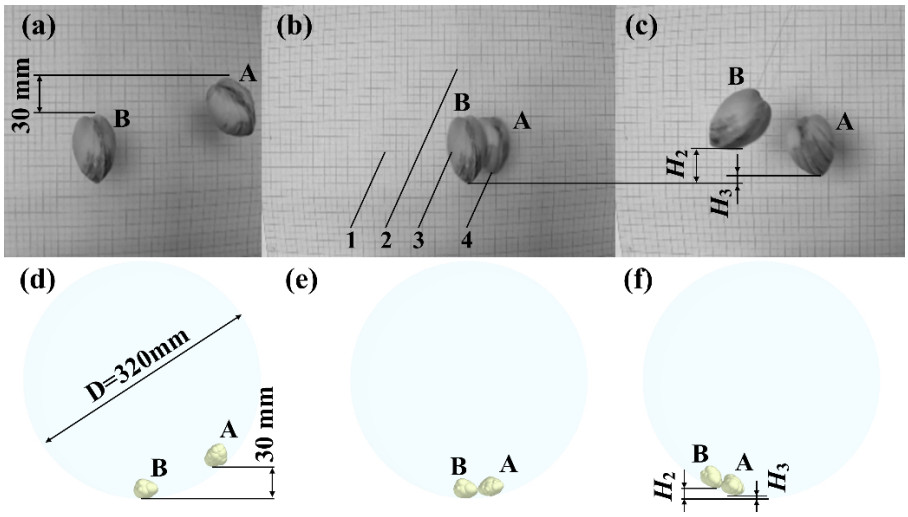


Figure 2. Physical and DEM collision processes for *M. veneriformis* restitution calibration. **a-c)** Physical experiment showing the initial, shell-shell impact, and post-collision state; 1. coordinate paper 2. long wire 3. M. veneriformis A 4. M. veneriformis B. **d-f)** Corresponding DEM simulation.

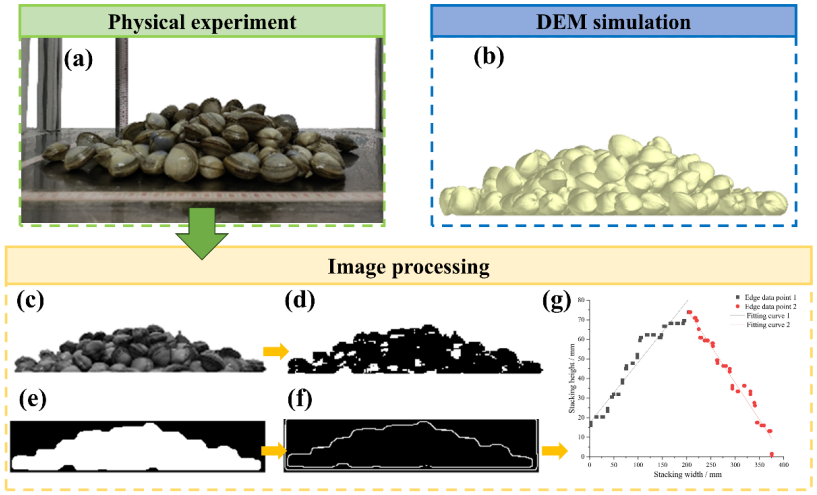


Figure 3. Measurement and image-processing procedure for AOR of *M. veneriformis*. **a)** Cylinder-lifting experiment. **b)** DEM simulation. **c)** grayscale image. **d)** Binarized image. **e)** Image segmentation. **f)** Edge detection. **g)** Edge-data-point fitting for AOR.

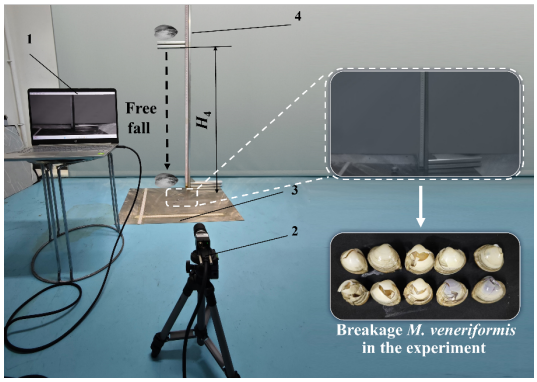


Figure 4. *M. veneriformis* drop-to-failure experiment. 1. laptop computer 2. high-speed camera 3. stainless steel base plate 4. test frame.

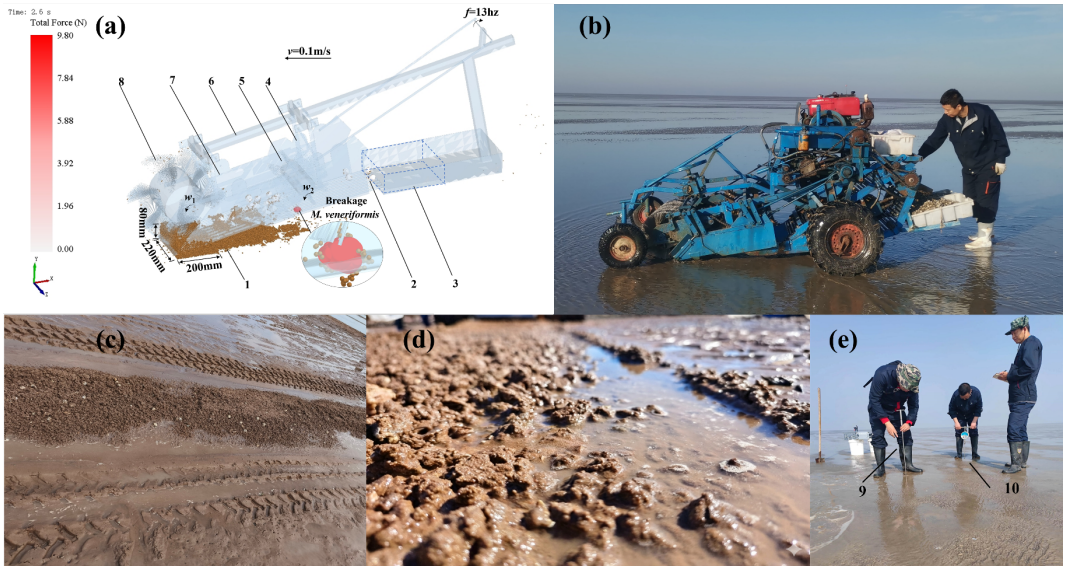


Figure 5. Validation of the *M. veneriformis* mechanized harvesting test and mudflat properties assessment. **a)** DEM–MBD harvesting simulation. **b)** Field harvesting test on the mudflat. **c)** Mudflat macro environment after harvesting. **d)** Mudflat micro environment after harvesting. **e)** Measurement of mudflat mechanical properties. 1. *M. veneriformis*-mudflat sediment mixture DEM model; 2. *M. veneriformis* DEM model; 3. collecting basket; 4. second-stage vibrating sieve; 5. second-stage sieving roller brush; 6. frame; 7. first-stage vibrating sieve; 8. first-stage double-spiral harvesting roller brush; 9. the vane shear tester; 10. the penetration resistance tester.

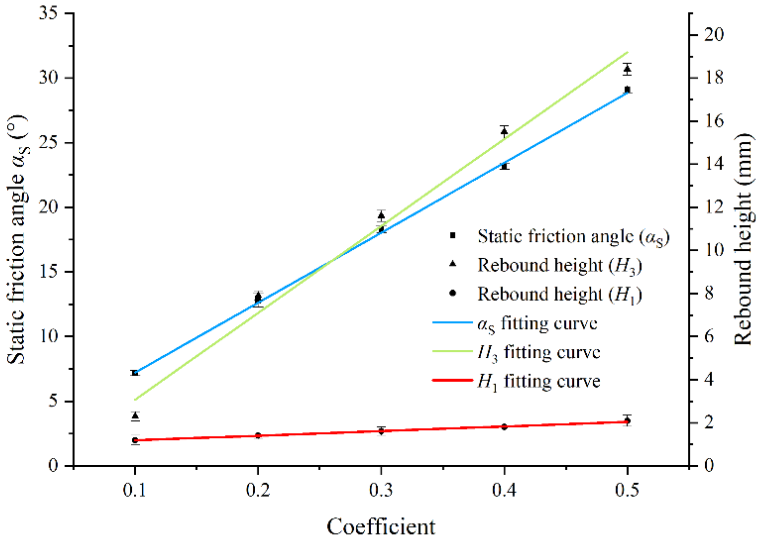


Figure 6. Single-factor calibration of *M. veneriformis* DEM contact parameters.

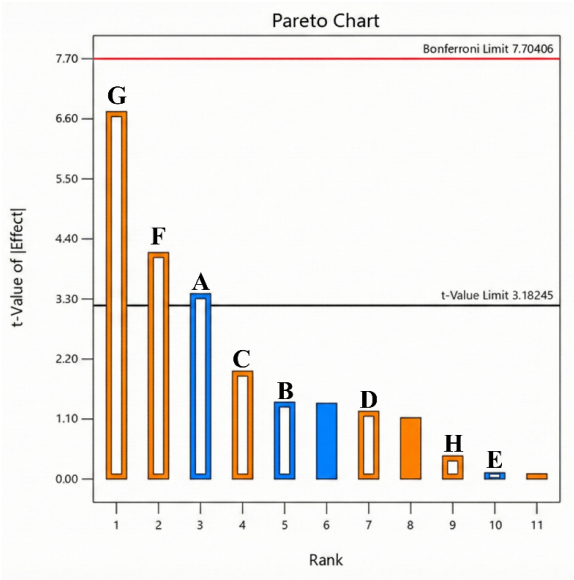


Figure 7. Pareto chart of the standardized effects of DEM parameters on the AOR in PBD. Orange means positive effects, blue mean negative effects. A, shell–shell surface energy; B, contact plasticity ratio; C, tension factor; D, tangential stiffness multiplier; E, shell–stainless steel rolling friction coefficient; F, shell–shell static friction coefficient; G, shell–shell rolling friction coefficient; H, shell–stainless steel surface energy.

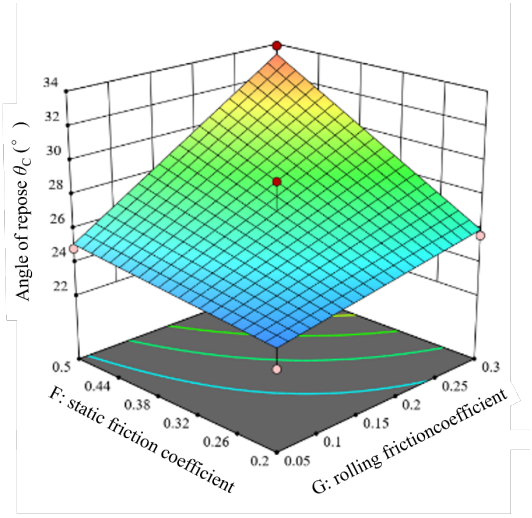


Figure 8. Effect of the interaction between the *M. veneriformis-M. veneriformis* rolling friction coefficient and static friction coefficient on the AOR.

Table 1. Measured physical and mechanical properties of *M. veneriformis.*

Parameter	Value	*CV* (%)
Length l_1 (mm)	37.14 ± 1.96	5.28
Height l_2 (mm)	25.58 ± 1.65	6.45
Width l_3 (mm)	32.59 ± 1.45	4.45
Volume V_C (cm³)	12.41 ± 0.67	5.40
Mass m_C (g)	17.68 ± 1.98	11.20
Density ρ_C (g cm-3)	1.43	–
Static friction angle α_s (°)	17.74 ± 1.95	10.99
Rebound height H_1 (mm)	10.51 ± 2.94	27.97
Rebound height H_3 (mm)	11.76 ± 3.44	29.25
Angle of repose θ_C (°)	22.21 ± 2.97	13.37
Breakage force $F_{b\text{-}C}$ (N)	9.1	–

Table 2. Comparison of physical measurements, calibrated DEM results, and mechanized harvesting validation results.

Validation stage	Parameter or response	Physical value	Simulation value	Relative error (%)
Contact-parameter calibration	*M. veneriformis*–stainless steel static angle, α_S (°)	17.74	17.22	2.93
	M. veneriformis–stainless steel restitution height (mm)	10.51	11.34	7.90
	M. veneriformis–M. veneriformis restitution height difference, H_2-H_3 (mm)	1.75	1.53	14.50
Macroscopic-response validation	AOR, θ_C (°)	22.26	23.17	4.09
Mechanized harvesting validation	Breakage rate, δ_B (%)	8.75	5.00	42.85
	Shell surface mud-attachment ratio, $W_{C–M}$	3.05	2.87	5.90

Table 3. DEM factors and levels in the AOR PBD simulation.

Factor	DEM parameter	Contact pair	Low-High level	Unit
A	Surface energy	*M. veneriformis–M. veneriformis*	0.10-2.00	J m^{-2}
B	Contact plasticity ratio	*M. veneriformis–M. veneriformis*	0.20-0.60	–
C	Tension factor	*M. veneriformis–M. veneriformis*	2.00-4.00	–
D	Tangential stiffness multiplier	*M. veneriformis–M. veneriformis*	0.40-0.80	–
E	Rolling friction coefficient	*M. veneriformis*–stainless steel	0.05-0.30	–
F	Static friction coefficient	*M. veneriformis–M. veneriformis*	0.30-0.70	–
G	Rolling friction coefficient	*M. veneriformis–M. veneriformis*	0.05-0.30	–
H	Surface energy	*M. veneriformis*–stainless steel	0.10-2.00	J m^{-2}

Table 4. Design and results of the AOR BBD simulation.

Run	G	F	A	θ_S (°)
1	0.050	0.20	1.05	22.67
2	0.300	0.20	1.05	25.62
3	0.050	0.50	1.05	24.83
4	0.300	0.50	1.05	33.89
5	0.050	0.35	0.10	26.39
6	0.300	0.35	0.10	30.39
7	0.050	0.35	2.00	24.60
8	0.300	0.35	2.00	29.40
9	0.175	0.20	0.10	25.62
10	0.175	0.50	0.10	29.82
11	0.175	0.20	2.00	24.57
12	0.175	0.50	2.00	27.25
13	0.175	0.35	1.05	28.82
14	0.175	0.35	1.05	26.86
15	0.175	0.35	1.05	26.56
16	0.175	0.35	1.05	26.42
17	0.175	0.35	1.05	22.67

G, *M. veneriformis–M. veneriformis* rolling friction coefficient; F, *M. veneriformis–M. veneriformis* static friction coefficient; A, *M. veneriformis–M. veneriformis* surface energy.

Table 5. ANOVA of the BBD regression model for the AOR.

Source	Sum of squares	df	Mean square	F-value	*p*-value
Model	106.72	6	17.79	19.23	<0.0001**
G	54.11	1	54.11	58.49	<0.0001**
F	37.43	1	37.43	40.47	<0.0001**
A	5.12	1	5.12	5.54	0.0405*
GF	9.33	1	9.33	10.09	0.0099**
GA	0.1580	1	0.1580	0.1708	0.6881
FA	0.5738	1	0.5738	0.6203	0.4492
Residual	9.25	10	0.9250		
Lack of fit	5.18	6	0.8641	0.8501	0.5918
Pure error	4.07	4	1.02		
Cor total	115.97	16			

*p<0.05; **p<0.01.

Table 6. Changes in physical and mechanical properties of mudflat sediment before and after harvesting.

Properties	Depth	Before harvesting	After harvesting
Sediment density ρ_S (kg m^{-3})	-	1892.78±53.47	1747.22±62.22
Water content W_w (%)	-	34.00±4.89	33.27±2.53
Shear strength τ_S (kPa)	50 mm	7.60±2.04	7.15±1.53
	70 mm	8.80±2.11	7.90±1.15
	100 mm	10.75±1.16	10.95±0.93
Penetration resistance F_r (N)	50 mm	1.57±0.42	0
	100 mm	5.71±0.53	0
	150 mm	17.43±0.97	1.60±0.33